Cloudy sky shortwave radiative closure for a Baseline Surface Radiation Network site

Ping Wang,[1] Wouter H. Knap,[1] and Piet Stammes[1]

Received 4 October 2010; revised 1 February 2011; accepted 7 February 2011; published 16 April 2011.

[1] A shortwave radiative closure analysis for cloudy skies is presented for the Cabauw Baseline Surface Radiation Network (BSRN) site (51.97°N, 4.93°E). The cloudy cases are carefully selected to be overcast, single-layer, homogeneous, nonprecipitating water clouds. We selected in total 639 cases on 9 days between May 2008 and May 2009 and on 30 January 2007. The Doubling-Adding KNMI (DAK) code is used to simulate global irradiances. The cloud optical thickness is derived from the cloud liquid water path from microwave radiometer (MWR) measurements and the MODIS L2 cloud effective radius product. The scattering phase matrix of the cloud particles is calculated using a Mie code with the two-parameter Gamma size distribution. The MWR integrated water vapor column and an aerosol climatology are also used in the simulations. The cloudy cases cover a large range of liquid water path (30–400 g/m^2), water vapor column (0.7–3.1 cm), and solar zenith angle (41°–75°). The mean difference between simulated global irradiances and BSRN measurements is 6 W/m^2 (5%), with a standard deviation of 14 W/m^2 (13%). This difference is within the uncertainties of the model input parameters and measurement errors. The correlation coefficient between the measured and simulated global irradiances is 0.95. The good closure results demonstrate the high quality of the MODIS effective radius data and MWR liquid water path data and the accuracy of the DAK model for the selected water cloud cases. Furthermore, the effects of clouds, aerosols, water vapor, and surface albedo on the global irradiance have been analyzed carefully. The sensitivity study shows that in order to achieve the closure with an uncertainty of a few W/m^2, more frequent effective radius data, simultaneous aerosol and cloud measurements, and surface albedo measurements are essential.

Citation: Wang, P., W. H. Knap, and P. Stammes (2011), Cloudy sky shortwave radiative closure for a Baseline Surface Radiation Network site, *J. Geophys. Res.*, *116*, D08202, doi:10.1029/2010JD015141.

1. Introduction

[2] Clouds have a significant influence on the Earth's radiation budget. Small changes in cloud parameters can have a large effect on the climate response associated with the changes in greenhouse gases, anthropogenic aerosols, or other factors [*Stephens*, 2005]. The study of cloud radiative closure (the difference between calculated and measured shortwave or longwave radiation) is important for the fundamental understanding of the interaction between clouds and radiation. A closure study is also of importance in order to evaluate cloud properties which have to be retrieved prior to the radiative transfer calculations. Thus, it is an important tool to evaluate the accuracy of cloud property retrievals and measurement techniques. The radiative transfer (RT) model can also be validated through a closure study using well-defined cases and high-quality measurements. *Oreopoulos and Mlawer* [2010] describe the current activities on the intercomparison of radiation codes, where the RT model simulations are compared with high-quality ground-based radiation measurements for well-defined clear-sky and overcast cases. The validated RT model and knowledge gained from the closure study can contribute to the parameterization of RT calculations in Global Climate Models (GCMs) [*Oreopoulos and Mlawer*, 2010].

[3] Several shortwave closure studies for cloudy cases have been performed during measurement campaigns, especially recently at the Atmospheric Radiation Measurement (ARM) sites. In order to study the cloud absorption anomaly [*Stephens and Tsay*, 1990] the second ARM Enhanced Shortwave Experiment (ARESE II) was conducted at the Southern Great Plains (SGP) site in February-April 2000. Using data from ARESE II, *Ackerman et al.* [2003] found that for three cloudy days, the measured and model calculated broadband shortwave atmospheric absorption agreed very well with each other. On 2 of the 3 days the calculations agreed with the measurements within 20 W/m^2 or less for a total column absorption of more than 200 W/m^2, thus better than 10%. On the third day, the model and measurements agreed within either 8% or 14% depending on which value

[1]Royal Netherlands Meteorological Institute, De Bilt, Netherlands.

0148-0227/11/2010JD015141

of the surface albedo was used. *Ackerman et al.* [2003] constrained the effective droplet radius by fixing the liquid water path from the microwave radiometer (MWR) measurements and then varying the effective radius in order to match the solar broadband flux at the ground. *Mace et al.* [2006] reported that for the year 2000 in uniform overcast skies at the SGP/ARM site, the calculations were strongly correlated to the measurements, with biases in the global irradiances at the surface and the top of the atmosphere of less than 10% and median relative errors ranging from 20% to as low as 2%. *McFarlane and Evans* [2004] examined shortwave closure for the Nauru and Manus Tropical Western Pacific (TWP) ARM sites for all-sky cases. They found that modeled global irradiances were unbiased with respect to the observed global irradiances while direct irradiances were underestimated and diffuse irradiances were overestimated.

[4] The most recent shortwave closure study for the single-layer, water clouds for overcast skies has been reported by *Nowak et al.* [2008] for the Baseline Surface Radiation Network (BSRN) site of Payerne, Switzerland. The authors obtained good agreement between measurements and simulations of less than 1% by adjusting the vertical extinction (optical thickness) in the modeled cloud layer within reasonable limits for stratus clouds. In order to validate the retrieved cloud optical thickness and effective radius from ground-based measurements, *Brandau et al.* [2010] compared the transmittances at 413 nm calculated with the Doubling-Adding KNMI (DAK) model to the transmittances derived from MultiFilter Rotating Shadowband Radiometer (MFRSR) observations. *Brandau et al.* [2010] found a good agreement between the simulated and measured transmittances with a bias of around 5%.

[5] In the Netherlands, the CESAR (Cabauw Experimental Site for Atmospheric Research) observatory consists of a large suite of instruments designed for studying the atmosphere and its interaction with the land surface. Since 2005, the radiation site of Cabauw has been part of the Baseline Surface Radiation Network [*Ohmura et al.*, 1998; *Knap*, 2008]. In May 2008 the Intensive Measurement Period At the Cabauw Tower (IMPACT), an activity of the European Integrated project on Aerosol Cloud Climate and Air Quality Interactions (EUCAARI), was held at Cabauw. For an exceptional period of cloudless weather during the first half of the campaign, *Wang et al.* [2009a] obtained excellent shortwave broadband irradiance closure. The radiative transfer calculations were performed with the Doubling-Adding KNMI (DAK) model [*De Haan et al.*, 1987; *Stammes*, 2001; *Kuipers Munneke et al.*, 2008; *Wang et al.*, 2009b], using Aerosol Robotic Network (AERONET) products for the characterization of aerosols and water vapor. The mean differences between model calculations and measurements were 2 W/m^2 (+0.2%) for the direct irradiance, 1 W/m^2 (+0.8%) for the diffuse irradiance, and 2 W/m^2 (+0.3%) for the global irradiance. This result is comparable to the results obtained by *Michalsky et al.* [2006].

[6] In the present work, we analyze the shortwave closure for overcast, single-layer, homogeneous, nonprecipitating water cloud cases at the Cabauw site. The diversity and variability of clouds is a challenge for radiative transfer model simulations and cloud retrievals. Therefore, we select simple cloud cases to limit the uncertainties of the model input parameters. Because of the good performance of the DAK model in the clear-sky closure study by *Wang et al.* [2009a] and in the narrow band cloudy closure study by *Brandau et al.* [2010], we continue to evaluate the performance of the DAK model for broadband shortwave irradiances in cloudy cases. In order to calculate global irradiances for cloudy cases, the DAK model needs cloud optical thicknesses, cloud scattering phase matrices, aerosol optical properties, water vapor data, and surface albedo data as input. The cloud optical thicknesses are derived from the liquid water path (LWP) observed by the ground-based MWR in Cabauw and the cloud effective radius observed by the MODIS satellite instrument. The integrated water vapor column data are also taken from the MWR. The aerosol information is taken from climatological AERONET data. The effects of cloud properties, aerosols, water vapor, and surface albedo on global irradiances are analyzed carefully to estimate the uncertainties in the simulated global irradiances. Compared to the clear-sky cases, the DAK simulations are quite slow for cloudy cases, because a large number of Gauss-Legendre division points (quadrature angles) are needed to get accurate results. Therefore, we use a look-up table approach for the simulations of the broadband shortwave global irradiances.

[7] The structure of the paper is as follows. Section 2 contains the methodology and data description, including the selection of cloudy cases, cloud properties and radiative transfer simulations. The results are shown in section 3. The effects of cloud properties, aerosol, water vapor, and surface albedo on the surface global irradiances and an uncertainty analysis are discussed in section 4. Conclusions are drawn in section 5.

2. Data and Methodology

2.1. Selection of Cloudy Cases

[8] The cloudy cases were selected between May 2008 and May 2009 using the Cloudnet target categorization product [*Illingworth et al.*, 2007], cloud fraction from the NubiScope and total sky imager, rain gauge data, and BSRN radiation measurements. All the instruments are located at the CESAR observatory. The selection criteria and data used for every selection step are listed in Table 1, and are discussed in detail below. Cloud fraction data from the NubiScope and rain gauge data were available every 10 min. Cloudnet data were provided for every 1 min. Therefore, the selection of the overcast, nonprecipitating, water clouds (steps 1–3) was performed for every 10 min interval. In the 10 min intervals we assumed that the cloud properties did not change. The global irradiances were calculated at 4 min intervals for all the cases that passed steps 1–3. Thus, we could simulate the diurnal cycle of the global irradiances and check the effects of multilayer and inhomogeneous clouds on the closure. Steps 4–5 were performed after the DAK simulations at 4 min intervals. So a cloud case refers to 4 min mean cloud properties. Step 6 was only used as a visual check but not used to select cases. The selection of cases was objective and all the cloudy cases were selected automatically according to steps 1–5. Although steps 4–5 were done after the DAK simulations, the simulated global irradiances were not used to select cases. We used visual checks for every step to make sure that the cases were selected properly.

Table 1. Steps for Selecting the Cloudy Cases

Steps	Criteria	Automated Selection	Visual Check
1	Overcast	NubiScope	TSI
2	No precipitation	Rain gauge, Cloudnet	Cloudnet
3	Water cloud	Cloudnet, MODIS	Cloudnet
4	Single-layer	Cloudnet	Cloudnet
5	No direct irradiance	BSRN	BSRN
6	Homogeneity	–	TSI, BSRN

[9] The essential instruments used for the Cloudnet target categorization are the vertically pointing cloud radar and backscatter lidar. Microwave radiometer (MWR) and rain gauge are recommended. The hourly model forecast data must be available (R. J. Hogan and E. J. O'Connor, Facilitating cloud radar and lidar algorithms: The Cloudnet Instrument Synergy/Target Categorization product, Cloudnet documentation, 2004, available at http://www.met.rdg.ac.uk/~swrhgnrj/publications/categorization.pdf). The target categorization algorithm makes use of the fact that the radar is sensitive to large particles such as rain and drizzle drops, ice particles, and insects, while the lidar is sensitive to higher concentrations of smaller particles, such as cloud droplets and aerosols [*Illingworth et al.*, 2007]. In the target categorization product, each pixel is categorized in terms of the presence of liquid droplets, ice, insects, aerosols etc. Cloud top and base heights are also provided in the product, with a temporal resolution of 15 s and a vertical resolution of 90 m from surface up to 11.5 km.

[10] The selection of cloudy cases was performed in the following steps:

[11] 1. Overcast is defined as cloud fraction of 1. We used cloud fractions derived from a NubiScope scanning IR radiometer, manufactured by IMK/Sattler-SES, with wavelength band 8–14 μm [*Wauben*, 2006]. The field of view of the IR radiometer is 3 degrees. The NubiScope performs every 10 min a scan of the whole sky which provides a total of 1080 brightness temperatures obtained during a scan at 30 zenith angles (1.5° to 88.5° in steps of 3°) and 36 azimuth angles (5° to 355° in steps of 10°). The NubiScope detects cloudiness when the atmospheric brightness temperature is above the clear-sky background. A visible Total Sky Imager (TSI, YES Inc.) was used to visually check the selected overcast cases. The cloud fraction database was created for 10 min intervals between May 2008 and May 2009 (http://www.knmi.nl/~savenije/BSRN/). More information about the cloud fraction detection is given by *Boers et al.* [2010].

[12] 2. Precipitation events were determined from rain gauge measurements. If the rain gauge recorded no precipitation, the case was further checked using the target categorization product and the rain flag from microwave radiometer measurements. When the rain gauge recorded no precipitation, we often saw drizzle from the Cloudnet target categorization product. These cases were flagged as no precipitation because the drizzle most probably did not reach the surface. The precipitation flag was generated at 10 min intervals with 1 h time lag and 20 min prelag. Therefore, if precipitation occurred at t_0, the entire time interval of $[t_0 - 20, t_0 + 60]$ minutes was flagged as precipitation. The time lags were used to make sure that the selected cases were not impacted by previous precipitation events.

[13] 3. Water clouds were selected from the Cloudnet target categorization product. Clouds with mixed liquid water and ice were excluded. At the time of a MODIS overpass (two times per day), cloud phase information from the MODIS level 2 product [*King et al.*, 1998] was used as an additional check. If the MODIS cloud phase product in a 0.2° × 0.2° box around Cabauw reported ice or mixed phase clouds, the case was rejected.

[14] 4. Single-layer clouds were checked automatically from the Cloudnet categorization data for every vertical bin. If two water cloud layers were separated by one bin, the case was flagged as a multilayer cloud, and was rejected.

[15] 5. For all cases that passed the first 4 checks we further limited them to having a direct irradiance of 0 (global and diffuse irradiances are equal). This also implies that we only select optically thick cloud cases, because the direct beam can only be blocked if the cloud optical thickness is larger than about 10 [*Bohren et al.*, 1995].

[16] 6. The homogeneity of clouds was visually checked using images from the Total Sky Imager and the BSRN downward longwave irradiance time series. For homogeneous clouds, the BSRN downward longwave irradiance normally shows a smooth curve, which also provides extra information with respect to the homogeneity of the clouds in space and time. On the TSI images, homogeneous clouds look smoother than nonhomogeneous clouds. There exists hardly any perfectly homogeneous cloud within the full field of view of the pyranometer. Therefore, we did not remove cases in step 6. Although the homogeneity criterion was not strictly satisfied for all cases, the information about the cloud homogeneity was used to understand the variation of the global irradiances.

[17] For the cases that passed selection steps 1–3, a continuity criterion was applied: if the cloud satisfied the selection steps 1–3 at a certain measurement time t_0, and was present continuously for 1 h ($t_0 \pm 30$ min) at each step, the case was selected. The continuity criterion might implicitly exclude some inhomogeneous cloud cases. It also helped to reduce the matching error between the measurements from the narrow field-of-view instruments (MWR, radar/lidar) and hemispherical viewing instruments (TSI, pyranometer). For all the cases the solar zenith angle (SZA) is less than 75°, because the plane-parallel DAK model was used for the simulations.

[18] The cloudy cases on 30 January 2007 have been used by *De Martino et al.* [2008] to study closure between the Regional Atmospheric Climate Model (RACMO) simulations and BSRN measurements. Because the same selection criteria were applied, we also included the 30 January 2007 cases to get more statistics.

2.2. Data Used in the Simulations

2.2.1. Cloud Data

[19] Cloud liquid water path (LWP) values were obtained from microwave radiometer (MWR) measurements. The KNMI HATPRO MWR served as primary instrument; in case of failure of HATPRO we used the RESCOM MWR, operated by European Space Agency (ESA). The cloud liquid water path and integrated water vapor column (IWV) are retrieved from both MWRs using a statistical method [*Loehnert and Crewell*, 2003]. The atmospheric brightness temperatures are measured at one frequency on the wing of

the water vapor line at 22.235 GHz and at a second frequency in the window region around 30 GHz. From measurements at both frequencies LWP and IWV can be retrieved simultaneously. For example, the frequencies 21.3 and 31.4 GHz are used to retrieve LWP and IWV from the RESCOM MWR. Seven frequencies between 22.24 and 31.4 GHz are used to retrieve LWP and IWV from HATPRO. The sampling rates are 1 or 2 s for HATPRO and 4 s for RESCOM. The MWRs are pointing to the zenith direction with a relatively narrow beam width of 3.5° HPBW (half power beam width) [*Rose et al.*, 2005]. Therefore, the cloud properties from the MWR narrow beam measurements may depart from the desired large area average that is impacting the BSRN global irradiance observations. Thus, the uniformity of the clouds is important. For the radiative transfer simulations, the LWP and IWV were averaged over 4 min (arithmetic mean), which corresponds to 160 measurements from HATPRO or 60 measurements from RESCOM. The aim of the averaging is to reduce the matching error due to the different fields of view between the MWR and the Pyranometer.

[20] The effective radii (r_e) of cloud droplets were taken from MODIS L2 data (MOD06_L2 and MYD06_L2) at 1 × 1 km^2 resolution. We used the MODIS effective radius retrieved from the 2.1 μm band. At Cabauw the daytime MODIS overpasses are around 1030 (Terra) and 1330 UTC (Aqua). We selected the closest overpass time for the cloud cases: if the selected cloud cases were in the morning we used MODIS data at 1030 UTC; if they were in the afternoon, we used the MODIS overpass data at 1330 UTC. For the cloud cases between the two MODIS overpass the effective radii were interpolated according to the measurement time. The MODIS data were collected over Cabauw within ±0.1° in latitude and longitude. For the selected cloud cases the MODIS data must also satisfy the selection criteria, so r_e must hold for water clouds. The distribution of r_e was derived from all r_e values in a 0.2° × 0.2° box for every MODIS overpass. The peak value in the distribution was selected as the optimal r_e. This selection approach for r_e could compensate for small variations of r_e in time and reduce the effects from extreme r_e values.

[21] In this closure study the cloud optical thickness (COT) was derived from independent instruments and wavelengths, therefore no implicit closure was involved. If the extinction efficiency (i.e., ratio of extinction cross section and geometric cross section) is assumed to be 2, the cloud optical thickness at visible wavelengths, τ_0, can be calculated according to

$$\tau_0 = \frac{3W}{2\rho r_e}, \tag{1}$$

where ρ is the density of liquid water, and W is the cloud liquid water path [*Stephens*, 1978]. In order to take into account the wavelength dependence of COT, the COT at other wavelengths (λ) was scaled using the ratio of the extinction efficiencies at λ and at 544.8 nm, the latter representing the visible wavelength:

$$\tau(\lambda) = \tau_0 \frac{Q(\lambda)}{Q(544.8\ \text{nm})}. \tag{2}$$

The extinction efficiencies Q were calculated by Mie theory together with the scattering matrices (see section 2.3), for every wavelength and value of r_e.

2.2.2. Atmospheric Profile

[22] In the simulations, the atmospheric state (pressure P, temperature T, water vapor and ozone profiles) was described by the midlatitude summer (MLS) profile given by *Anderson et al.* [1986]. The MLS atmospheric profile has 1 km vertical resolution from 0 to 25 km. Above 25 km, the levels are at 30, 35, 40, 45, 50, 70, 100 km. The 4 min averaged IWV data from MWR are used to scale the MLS water vapor profile. The deviation of actual P, T and ozone profiles from the MLS profiles have very small impact on the shortwave global irradiance for overcast cases, therefore we did not use the atmospheric profiles from radiosonde measurements.

2.2.3. Aerosol Data

[23] The aerosol information was taken from the LOWTRAN aerosol climatology [*Shettle and Fenn*, 1979]. The LOWTRAN aerosol data provide aerosol profiles (at the same altitude grid as the MLS atmospheric profile), single scattering albedos (SSA), asymmetry parameters (ASY) and extinction coefficients (EXT) at 47 wavelengths from 0.2 to 300 μm for several aerosol types (e.g., rural and urban type aerosols). ASY, SSA and EXT vary with relative humidity and the aerosol profiles depend on visibility. The most important settings for the LOWTRAN aerosols are: aerosol type, relative humidity (RH) and visibility (VIS) in the boundary layer (0–2 km), RH and VIS in the free troposphere (2–10 km), and AOT. The user can choose RH = 50, 70, 80, 99%, VIS = 50, 23, 10, 5, 2 km in the boundary layer and VIS = 23 or 50 km in the free troposphere. We scaled the LOWTRAN aerosol information with the AOT applicable to Cabauw.

[24] We used the AOT climatology for Cabauw from the AERONET data, because we did not have AERONET data on overcast days [*Dubovik et al.*, 2000]. For Cabauw the annual mean AOT is 0.23 at 500 nm with a standard deviation of 0.1. Aerosol properties often vary significantly from day to day; this implies that the yearly mean or monthly mean AOT may be quite different from the actual AOT. This is discussed in section 4.2.

2.2.4. Surface Albedo

[25] In the cloudy closure analysis we used the spectral surface albedo derived for a typical grass curve presented by *Bowker et al.* [1985]; the same data were used for the clear-sky closure analysis [*Wang et al.*, 2009a]. In order to study the impact of the spectral surface albedo on the simulated global irradiance, we simulated global irradiances using three different grass reflectance spectra (Grass-Fescue-Wheat YNP-FW-1, YNP-FW-2, YNP-FW-3) from the USGS Digital Spectral Library 06 [*Clark et al.*, 2007]. For grass spectra 1 and 2 the grass type is Idaho fescue and bearded wheatgrass; for grass spectrum 3 the type is Idaho fescue and bluebunch wheatgrass. *Popp et al.* [2011] compiled a new global surface albedo climatology based on Medium Resolution Imaging Spectrometer (MERIS) Albedomap data (http://www.brockmann-consult.de/albedomap/). The MERIS climatological surface albedo databases were generated at a grid of 0.25° × 0.25° (latitude × longitude) for each month of the year and for 13 different spectral channels between 412 and 885 nm. Because the spectral surface

Table 2. Settings for the Reference Irradiance LUT, Water Vapor Correction LUT, and Aerosol Correction LUT[a]

Parameter	Reference Irradiance LUT: G_{ref}	Water Vapor Correction LUT: G_{iwv}	Aerosol Correction LUT: G_{aer}
COT	0, 0.5, 0.6, 0.8, 1, 1.3, 1.6, 2, 2.5, 3.2, 4, 5.0, 6.4, 8, 10.1, 12.7, 16, 20.2, 25.4, 32, 40.3, 50.8, 64, 80.6, 101.6, 128, 161.3	10.1, 16, 32	10.1, 16, 32
r_e (μm)	2, 2.5, 3, 3.5, 4, 5, 6, 7, 8, 9, 10, 12, 14, 16, 18, 20	6, 8, 10	6, 8, 10
AOT	0	0	0.1, 0.2, 0.3
IWV (cm)	2.96	0.5, 1, 2, 4	2.96
O_3[b] (DU)	340		
CO_2[b] (ppm)	368		
μ_0[b]	0.259, 0.3, 0.4, 0.5, 0.6, 0.707, 0.8, 0.866, 0.940, 1.0		
Atmospheric profile[b]	Midlatitude summer		
Surface albedo[b]	Grass spectrum [*Bowker et al.*, 1985]		

[a]LUT, look-up table.
[b]These settings are the same for all LUTs.

albedo at Cabauw could be different from the four grass spectra, we compared the grass spectra with the climatological surface albedo values at Cabauw. We selected the MERIS surface albedo values in the grid box over Cabauw at 13 wavelengths.

2.3. Radiative Transfer Calculations

[26] The DAK model uses the doubling-adding method to calculate upward and downward radiation at every level of a multilayer plane-parallel atmosphere. It includes multiple scattering, gas absorptions, polarization, and different kinds of scattering phase matrices for cloud and aerosol particles. The atmospheric state (pressure, temperature, trace gas mixing ratio) and optical properties of particles (optical thickness, single scattering albedo, scattering phase matrix) are defined for each layer individually. In the doubling-adding scheme, integration of a multiplication of radiation field matrices, like reflection and transmission matrices, takes place. The azimuth dependence of the radiation field is treated as a Fourier expansion, so each Fourier term can be treated separately. The zenith angle integration is treated as a Gauss-Legendre integration. The number of Gauss-Legendre division points (also called quadrature angles) determines the accuracy of the doubling-adding scheme and the speed of calculations [*De Haan et al.*, 1987; *Stammes*, 2001]. In order to achieve an error of 10^{-5} in the reflectance and transmittance, which is less than 0.01 W/m^2 for the irradiance, sixty Gauss-Legendre division points were used in the computations. The original version of the DAK model is a line-by-line code, covering wavelengths from UV to near-IR. The k distribution method is implemented in DAK to calculate broadband solar irradiances [*Kuipers Munneke et al.*, 2008; *Wang et al.*, 2009b]. The global irradiances are calculated for 32 wavelength bands from 240 to 4600 nm using the k distribution coefficients for the absorptions by O_2, CO_2, O_3 and water vapor [*Kato et al.*, 1999]. The extraterrestrial total solar irradiance is 1365 W/m^2 and is corrected according to the Earth-Sun distance.

[27] For water clouds the scattering (phase) matrices were calculated using Mie theory [*De Rooij and van der Stap*, 1984]. The cloud scattering matrices were calculated at the central wavelength for each of the 32 wavelength bands using 14 different effective particle radii. The effective radius was varied from 2 to 20 μm and the effective variance was set to 0.15. The effective variance value was selected based on the measurements by *Diem* [1948]. The particle size distribution was assumed to be a two-parameter Gamma distribution [*Hansen*, 1971]. The complex refractive index of water was taken from *Segelstein* [1981]. The *Segelstein* [1981] data cover the wavelength range 0.01–10^7 μm with about 0.01 μm spectral resolution at visible and near-infrared wavelengths. Although several complex refractive index spectra are published, they are mainly for the visible wavelength range. For consistency, we only used data from *Segelstein* [1981].

[28] It takes about 50 min to calculate the global irradiance for one cloud case, which is too slow to process a large number of cases. To speed up the irradiance simulations, the irradiances were precalculated and stored in look-up tables (LUT). Three LUTs were generated: the reference irradiance LUT, and the water vapor and aerosol correction LUTs. The global irradiances stored in the LUTs are called G_{ref}, G_{iwv} and G_{aer}. The settings for the LUTs are summarized in Table 2. The input parameters of DAK are also presented in Table 2 except for r_e. The advantage of using three LUTs instead of including all the combinations of water vapor and aerosol settings in one LUT is that the size of the LUTs is smaller and the computation is faster.

[29] For the reference irradiance LUT, the surface global irradiances (G_{ref}) were precalculated at 27 cloud optical thicknesses (from 0 to 161), 14 effective radii (from 2 to 20 micron) and 10 cosines of solar zenith angle (μ_0 from 0.2588 to 1). The MLS atmospheric profile was used for the LUTs, with fixed CO_2 mixing ratio of 368 ppm and without aerosols. Thus in the reference irradiance LUT, the integrated water vapor column (IWV) is 2.96 cm and the O_3 column density is 340 DU. The IWV and aerosols were corrected later in the water vapor and aerosol correction LUTs. The cloud was assumed to be a homogeneous layer located between 1 and 2 km altitude, because cloud height is not important for the shortwave global irradiance at the surface [*Schmetz*, 1993].

[30] The water vapor and aerosol correction LUTs were constructed to correct G_{ref} for the actual integrated water vapor (IWV) column amount and aerosol optical thickness (AOT), respectively. The correction LUTs have the same settings as the reference irradiance LUT but with different IWV or AOT and with less number of COT and r_e values. In the water vapor correction LUT (G_{iwv}), IWV was set to 0.5, 1.0, 2.0, 4.0 cm and the profile shape is the MLS water

Table 3. Mean Differences ($\langle \Delta G \rangle$) Between the Simulated (G_{sim}) and Measured (G_{meas}) Global Irradiances for All the Cloudy Cases[a]

Date	G_{meas} (W/m^2)	$\langle \Delta G \rangle$ (W/m^2)	σ (W/m^2)	R	Minimum μ_0	Maximum μ_0	N	Case
30 Jan 2007	87.2	4.4	6.1	0.974	0.251	0.348	157	1–157
15 Jul 2008	61.3	14.9	4.1	0.980	0.285	0.433	11	158–168
26 Aug 2008	110.5	11.1	16.5	0.957	0.261	0.745	88	169–256
28 Aug 2008	155.1	23.4	19.5	0.948	0.355	0.738	63	257–319
29 Aug 2008	112.7	−3.2	11.5	0.977	0.351	0.628	35	320–354
24 Sep 2008	73.0	1.0	13.2	0.923	0.252	0.411	28	355–382
6 Oct 2008	138.5	−3.7	16.3	0.878	0.410	0.540	43	383–425
7 Oct 2008	126.3	0.4	15.4	0.889	0.481	0.535	28	426–453
4 Nov 2008	110.8	2.6	8.2	0.935	0.252	0.383	186	454–639
All	109.5	5.6	14.0	0.949	0.251	0.745	639	–

[a]Here σ is the standard deviation of $\langle \Delta G \rangle$, R is the correlation coefficient, and N is the number of cases per day and in total.

vapor profile. Aerosol was not included in the water vapor correction LUT. For the aerosol correction LUT (G_{aer}), the LOWTRAN rural type aerosol [*Kneizys et al.*, 1988] was used, because Cabauw is located in a rural area. The aerosol settings were as follows. In the boundary layer (0–2 km) the relative humidity (RH) was 99% and the visibility (VIS) was 10 km. The free tropospheric RH was 70% and VIS was 50 km. With the above LOWTRAN aerosol settings, for a total AOT of 0.2 (at 500 nm), the DAK model provides the layer mean values for AOT and aerosol single scattering albedo (SSA). The boundary layer has AOT = 0.172 and SSA = 0.986, and the free troposphere has AOT = 0.026 and SSA = 0.964. With the same RH and VIS settings, the aerosol correction LUT (G_{aer}) was created for AOT values of 0.1, 0.2 and 0.3 at 500 nm. The MLS water vapor profile (IWV = 2.96 cm) is used in the aerosol correction LUT.

[31] To find the simulated irradiance G_{sim} from the three LUTs, first the reference irradiance is interpolated from the reference irradiance LUT using COT, r_e, and μ_0, leading to G_{sim_ref}. Then, the aerosol correction of the reference irradiance, ΔG_{sim_aer}, is calculated by interpolating $\Delta G_{aer} = G_{aer} - G_{ref}$ as a function of AOT, COT, r_e, and μ_0. Next, the integrated water vapor correction of the reference irradiance, ΔG_{sim_iwv}, is calculated by interpolating $\Delta G_{iwv} = G_{iwv} - G_{ref}$ as a function of IWV, COT, r_e, and μ_0. Finally, the simulated global irradiance is the sum of the three terms, namely,

$$G_{sim} = G_{sim\_ref} + \Delta G_{sim\_aer} + \Delta G_{sim\_iwv}. \quad (3)$$

2.4. Surface Radiation Measurements

[32] Surface radiation measurements at the Cabauw BSRN site were used in this closure study. This means that the radiation measurements used for the closure study were made according to the highest available standards [*Ohmura et al.*, 1998; *McArthur*, 2004]. The estimated uncertainties in the direct, diffuse, and global irradiance, as achieved by BSRN in 1995, are ±2 W/m^2, ±5 W/m^2, and ±5 W/m^2, respectively. These values represent calibration uncertainties, which mean that operational uncertainties, referring to field conditions, are generally larger. *Shi and Long* [2002] estimated the operational uncertainties for BSRN-type measurements to be typically ±(14 ± 6) W/m^2 for the direct irradiance and ±(9 ± 3) W/m^2 for the diffuse irradiance.

[33] The simulated global irradiances (G_{sim}) were compared with the instantaneous BSRN measurements (G_{meas}). The DAK simulated global irradiances were calculated at the mean of the LWP measurement time in a 4 min interval. The BSRN data were linearly interpolated to the mean of the LWP measurement time. Because of the high time resolution of the BSRN measurements (1 min), the effect of the temporal interpolation is small. The difference between simulated and measured global irradiances at this time represents the radiative closure:

$$\Delta G = G_{sim} - G_{meas}. \quad (4)$$

According to the uncertainty of the BSRN measurements, for a good closure ΔG should be less than 12 W/m^2, i.e., the accuracy of the diffuse irradiance for instantaneous data.

3. Results

[34] For the period of May 2008 to May 2009, between 0700 and 2000 local time, there are 28470 cloud fraction data points from the NubiScope measurements. After the selection steps 1–3, 2258 overcast, nonprecipitating 10 min interval cases remain, where the ice clouds are 1474 cases and water clouds are 691 cases. 93 cases cannot be classified because of missing Cloudnet data. As mentioned in section 2.1, the 10 min interval water cloud cases are redefined to 4 min interval cases to be used in the radiative transfer calculations. After selection steps 4 and 5 we have 639 4 min interval cloud cases on 9 days in the period May 2008 to May 2009 and on 30 January 2007. The closure analysis results for the 639 cases are presented in Table 3. The global irradiances, LWP and IWV for 4 November and 26 August 2008 are shown in Figure 1 as an example.

[35] There are 186 cases on 4 November 2008. As shown in Figure 1a the global irradiance values are relative low and have small variations. The variation of the global irradiance mainly follows the variation of the solar zenith angle. The range of μ_0 for these cases is [0.252, 0.383]. Although the COT is only about 10–15 on this day, the global irradiance values are quite low due to the large solar zenith angle. Figure 1e shows the LWP and IWV for these cases. The range of LWP is [49.78, 81.28] g/m^2 with a mean value and standard deviation of 58.22 g/m^2 and 6.37 g/m^2, respectively. The range of the IWV is [1.77, 1.87] cm, with a mean of 1.83 cm and a standard deviation of 0.02 cm. Some simulations between 1200 and 1300 UTC are excluded because of the presence of cirrus clouds above the water clouds. The difference between the simulated and measured global irradiances is 3 W/m^2 with a standard deviation of

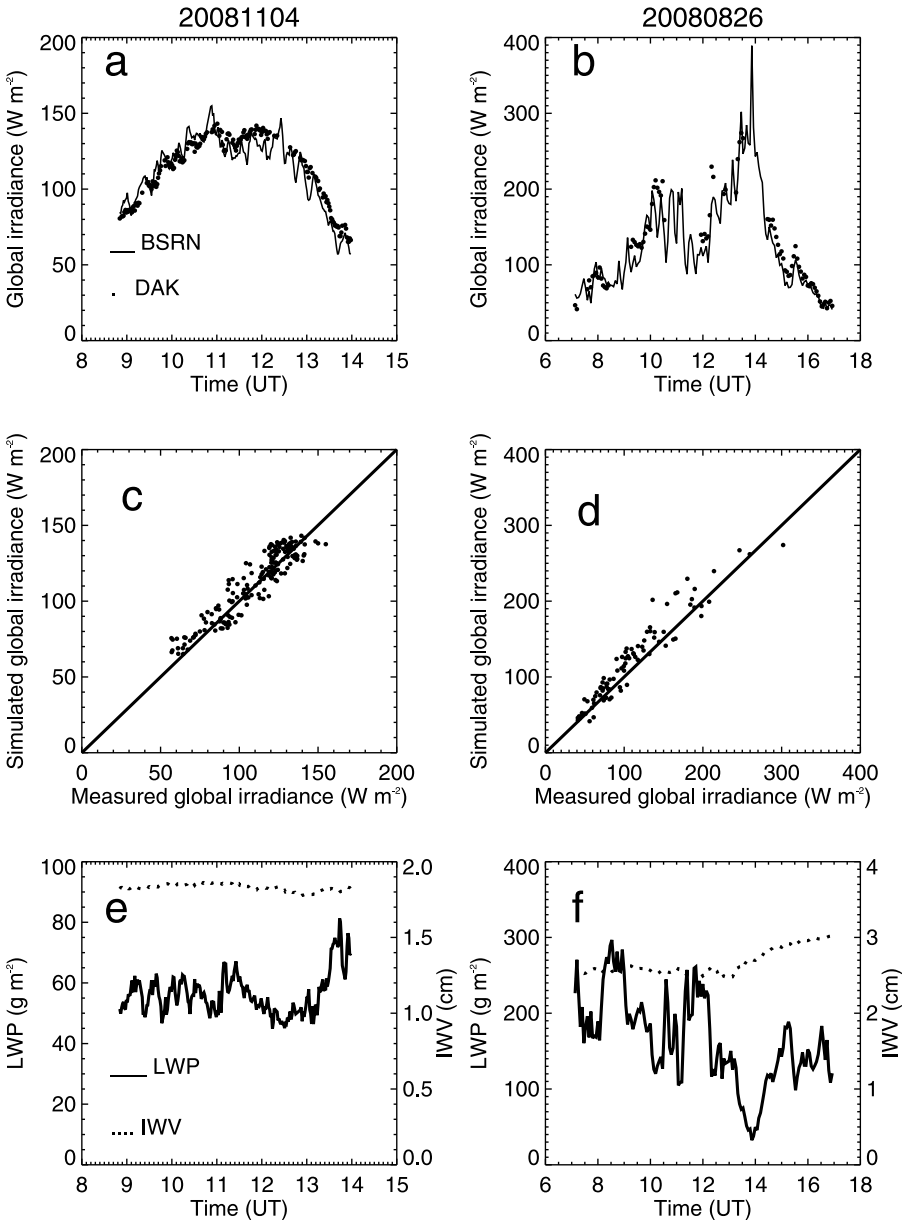

Figure 1. Results for (a, c, e) 4 November and (b, d, f) 26 August 2008. Figures 1a and 1b show the global irradiances from BSRN measurements at Cabauw (solid line) and the DAK simulations (solid circles). Figures 1c and 1d show scatterplots of simulated versus measured global irradiances. The solid line indicates the one-to-one line. Figures 1e and 1f show the cloud liquid water paths (solid line, left y axis) and integrated water vapor columns (dotted line, right y axis).

8 W/m^2. The correlation coefficient between the simulated and measured global irradiances is 0.935 (see Figure 1c).

[36] As shown in Figure 1b, on 26 August 2008 the variation of the global irradiance (88 cases) is larger than that on 4 November. Figure 1f illustrates that on 26 August LWP (IWV) values are larger and are more variable than the LWP (IWV) on 4 November. According to the TSI images the clouds on 26 August are not as homogeneous as the clouds on 4 November. Between 1200 and 1400 UTC there are no simulations because of the presence of broken clouds; this can be seen from the increase in global irradiance and decrease in cloud water path. Other missing cases in the simulations are due to the presence of cirrus clouds above the water clouds. Between 1400 and 1600 UTC, the simulated global irradiances have a positive bias. The bias might be due to the uncertainty of the effective radius. At the MODIS overpass time, around 1330 UTC, there are broken clouds; consequently r_e derived from these clouds might not reflect the particle size for the clouds present later in the day. The difference between the simulated and measured global irradiances is 11 W/m^2 with a standard deviation of 16 W/m^2. The simulated and measured global irradiances have a good correlation with a correlation coefficient of 0.957 (see Figure 1d).

[37] As presented in Table 3, 67% of the cases are on 30 January 2007, 26 August 2008 and 4 November 2008.

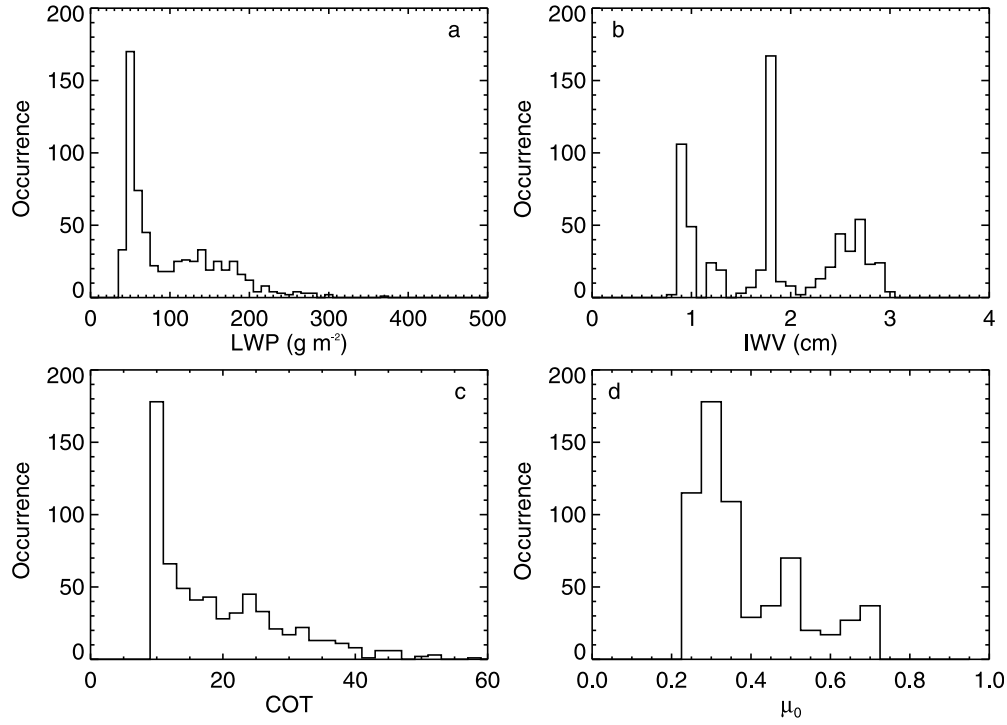

Figure 2. Histograms of (a) cloud liquid water path (LWP), (b) integrated water vapor column (IWV), (c) cloud optical thickness (COT), and (d) cosine of solar zenith angle (μ_0) for all the cloud cases.

The bias and standard deviation are smaller on 30 January 2007 and 4 November 2008 than on other days. The lowest correlation coefficient between simulated and measured global irradiances is 0.878. The largest $\langle \Delta G \rangle$ (23.4 W/m^2) occurs on 28 August 2008 with the standard deviation of 19.5 W/m^2. However, the correlation coefficient on this day is still high, 0.948. This suggests that the cloud variations are characterized properly by the LWP. Most probably r_e is too large, thus the COT is too small. If there would have been a large error in LWP, a similar bias might occur on other days.

[38] For the complete set of 639 cases, the cloud liquid water path and integrated water vapor span a wide range, because the cases occur in summer and winter. The distributions of LWP, IWV, COT and μ_0 are shown in Figure 2. The LWP varies from 30 to 400 g/m^2 but 57% of the values are less than 100 g/m^2. The mean LWP is 106.2 g/m^2 with a standard deviation of 58.9 g/m^2. The COT distribution is very similar to the LWP distribution, with a mean of 20.1 and standard deviation of 9.7. The range of r_e is 6.5–10 μm with a mean of 7.9 μm. The IWV range is from 0.7 to 3.1 cm. The mean and standard deviation of IWV are 1.9 cm and

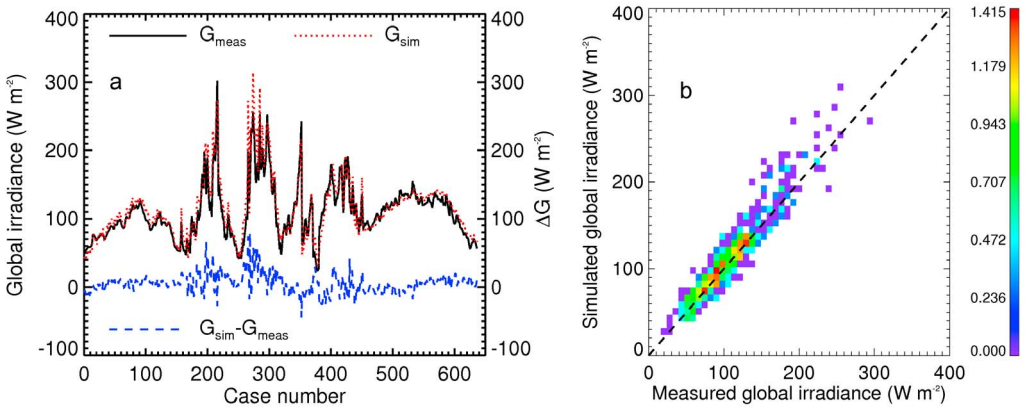

Figure 3. (a) Time series of the simulated (G_{sim}) and measured (G_{meas}) global irradiances and the differences $\Delta G = G_{sim} - G_{meas}$ (right y axis) for all the selected cases. (b) Scatter density plot of simulated and measured global irradiances for all the selected cases. The color indicates the number of the cases on a logarithmic scale. The dashed line is the one-to-one line.

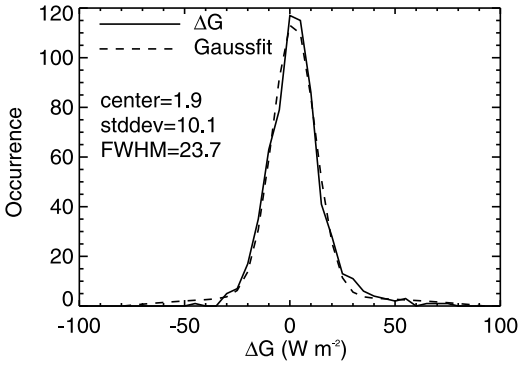

Figure 4. Distribution of the differences between simulated and measured global irradiances (ΔG) for all the selected cases and the Gaussian fit. The unit for the center, standard deviation, and full width half maximum (FWHM) is W/m^2.

0.7 cm, respectively. The solar zenith angles are between 41° and 75°.

[39] The global irradiances for all the cases are chronologically presented in Figure 3a and the scatter density plot is shown in Figure 3b. The case number for each day is given in Table 3. The largest differences appear close to case number 200 and 300 on 26 and 28 August 2008. The best closures occur at case numbers 1–150 and 450–639. The simulated global irradiances and BSRN measurements are in good agreement for most cases, especially for the lower irradiance values. The mean difference $\langle \Delta G \rangle$ is 6 W/m^2 (5%) and the standard deviation σ is 14 W/m^2 (13%). This is a good closure result when compared to the BSRN measurement accuracy (see section 2.4). As shown in Figure 3b the largest number density in the scatterplot is close to the one-to-one line. There are a few outliers at high irradiance values. The distribution of the global irradiance differences ΔG and its Gaussian fit are illustrated in Figure 4. The mean, standard deviation and full width half maximum (FWHM) of the Gaussian fit are 1.9, 10.1 and 23.7 W/m^2, respectively. The mean and standard deviation of the Gaussian fit are smaller than $\langle \Delta G \rangle$ and σ, respectively, which indicates that a few large ΔG values contribute significantly to the mean and standard deviation.

[40] We also examined the dependence of ΔG on COT and μ_0. As shown in Figure 5, ΔG does not depend on the COT and μ_0, although at large μ_0 some simulated values are larger than the BSRN measurements. Since there are only a few measurements at large μ_0, we cannot conclude that the correlation between ΔG and μ_0 is statistically significant.

4. Sensitivity Study and Discussion

[41] In the sensitivity study of this section we investigate the effects of cloud properties, aerosols, water vapor and surface albedo on the global irradiances and try to quantify the uncertainty of the simulated global irradiances. Because we use separated correction LUTs for water vapor and aerosols, also a sensitivity study of the accuracy of this approach is performed.

4.1. Effect of Cloud Properties

[42] Simulations of the global irradiance at $\mu_0 = 0.5$ are shown in Figure 6 for different values of COT and r_e. The global irradiance at the surface decreases with increasing cloud optical thickness and slightly increases with increasing effective radius. For the selected cloud cases the COT range is 10–60 and the range of r_e is 6–10 μm. As shown in Figure 6, in these COT and r_e ranges the global irradiance is more sensitive to COT than to r_e. Therefore the errors in COT cause the largest uncertainty in global irradiances. In our simulations r_e has two effects on the global irradiances:

[43] 1. The scattering matrix depends on r_e. Large particles have a stronger forward scattering peak than small particles; therefore the global irradiance is larger for large r_e.

[44] 2. Because r_e is used to calculate the COT with equation (1), the error in r_e directly leads to an error in COT. These two effects are further discussed in section 4.6 with DAK simulations.

[45] The MODIS near-infrared bands at 1.6 μm, 2.1 μm and 3.75 μm are sensitive to the cloud droplets at different depths within the cloud [*Platnick*, 2000]. The effective radius retrieved from the 3.75 μm band is close to the droplet size at the top of the cloud. The 2.1 μm and 1.6 μm bands are more sensitive to the droplets deeper inside the cloud. For water clouds, especially nonprecipitating water clouds, the effective radius almost linearly increases from cloud base to cloud top [*Miles et al.*, 2000; *Chen et al.*,

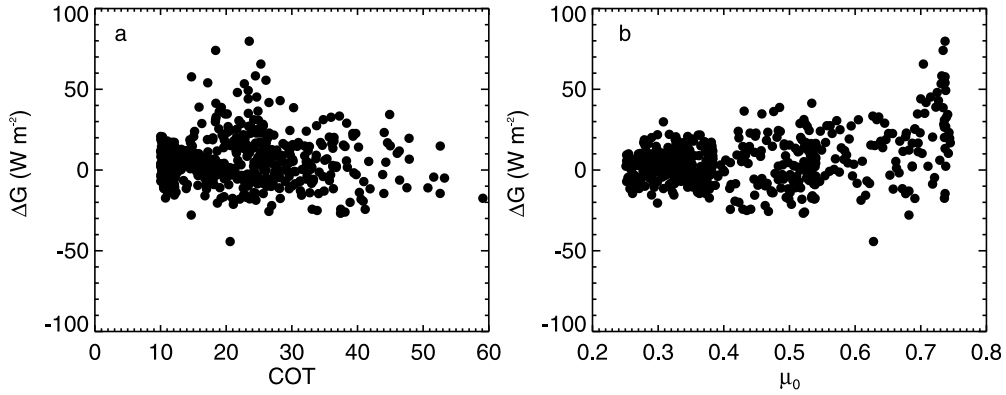

Figure 5. The differences between the simulated and measured global irradiances (ΔG) as a function of (a) cloud optical thickness (COT) and (b) cosine of solar zenith angle (μ_0) for all the selected cases.

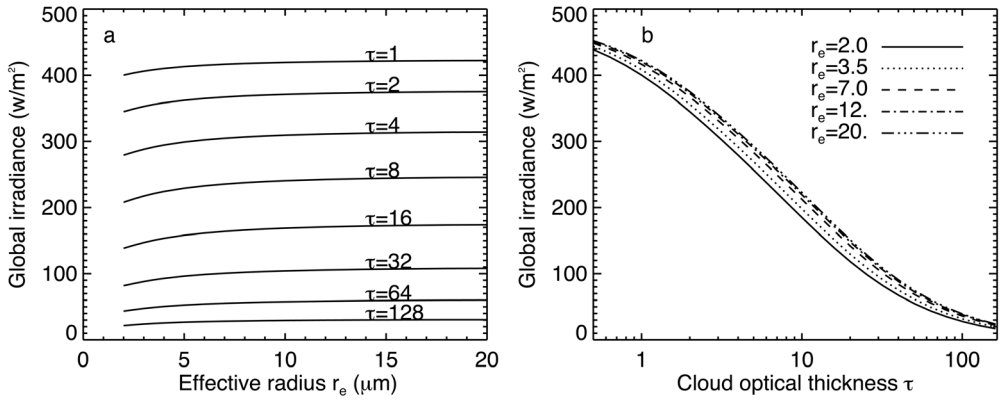

Figure 6. (a) Global irradiance at the surface varied as a function of effective radius (r_e) for different cloud optical thicknesses (τ) for water clouds. (b) Global irradiance at the surface varied as a function of τ, for different values of r_e (in μm). In both plots, $\mu_0 = 0.5$.

2008]. Therefore, r_e values from the 2.1 μm band are more suitable for being used to calculate COT for the cloud layer than r_e values from the 3.75 μm band.

[46] We only have one or two effective radii from MODIS per day to calculate the optical thickness for the cases with several hours' time difference (normally less than 6 h). One of the critical assumptions is that the variation in the effective radius is small and the variation in the global irradiance is dominated by the variation in the liquid water path. This assumption is confirmed by *Sengupta et al.* [2003]. Using 1 year of overcast cloud cases at the SGP/ARM site, they find that surface radiation has a higher sensitivity to cloud liquid water path variations than to cloud droplet effective radius variations. Liquid water path variations can cause three times more variation in optical thickness than effective radius can. They explain that this higher sensitivity of solar irradiances to liquid water path is a result of the regimes of natural occurrence of cloud liquid water paths and cloud droplet effective radii. In our cloud cases, the maximum value of r_e is only 1.6 times its minimum value, while the maximum value of LWP is 12 times its minimum value.

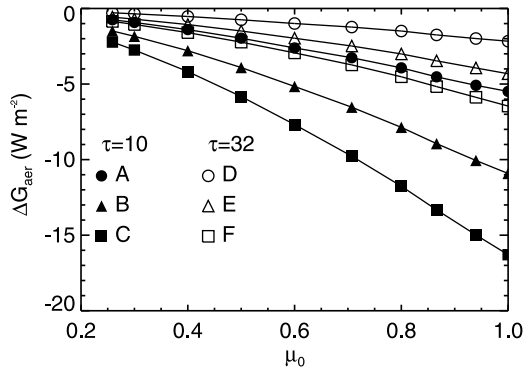

Figure 7. Sensitivity of global irradiance to AOT as a function of μ_0. ΔG_{aer} is the difference between the global irradiance calculated with AOT = 0.1 (circles labeled A and D), 0.2 (triangles labeled B and E), and 0.3 (squares labeled C and F) and the global irradiance calculated with AOT = 0, for cloud optical thickness of 10 (symbols A-C) and 32 (symbols D-F). $r_e = 8$ μm.

[47] The cloud height has a very small effect on the global irradiance (G) at the surface. *Schmetz* [1993] has demonstrated that the surface net flux (NET_{srf}) decreases from 616 W/m^2 for a thin cloud (COT = 5.7) at 1 km to 604 W/m^2 for the same cloud at 13 km assuming a surface albedo (α) of 0.2 and $\mu_0 = 1$. According to *Schmetz* [1993], $NET_{srf} = (1 - \alpha) * G$. In our case the cloud top heights are mainly below 2 km, therefore the cloud top height differences between the DAK model setting and the actual cloud top height could be about 1 km. Additionally, the global irradiances are relative low (<300 W/m^2) in our case due to the large COT and small μ_0. Therefore, we estimate that the error due to the fixed cloud height in our closure study is less than 1 W/m^2. The geometric thickness of the single cloud layer is not important because in the DAK model the calculations are performed according to the optical thickness of every model layer. Although cloud layers are often thinner than 1 km [*Crewell et al.*, 2009], the assumption of a cloud layer at 1–2 km does not cause a significant uncertainty, whereas the LUTs are much simpler with a fixed cloud layer height.

4.2. Effect of Aerosols

[48] For cloudy cases the vertical distribution of aerosols is more important than for clear sky cases, because the long scattering light path inside the clouds can enhance the small absorption by the aerosols. Using the LOWTRAN aerosol profile, the boundary layer aerosol is half inside the cloud layer and half below the cloud layer. In terms of absolute values, the effect of aerosols on the global irradiance is more pronounced in the clear-sky cases than in the cloudy cases. At $\mu_0 = 0.42$, changes in AOT of ±0.02 lead to changes in the global irradiance of ±5.2 W/m^2 for clear-sky cases and of ±0.44 W/m^2 for cloudy cases (see Table 5).

[49] According to the daily Absorbing Aerosol Index images from GOME-2 (Global Ozone Monitoring Experiment; see http://www.temis.nl/airpollution/absaai) there are no elevated absorbing aerosols (e.g., smoke or desert dust) present in the selected cases, so we can only consider rural or industrial types of aerosol, which are mainly in the boundary layer. Probably it is reasonable to use the rural aerosol type in this closure study. The cloud particle size in

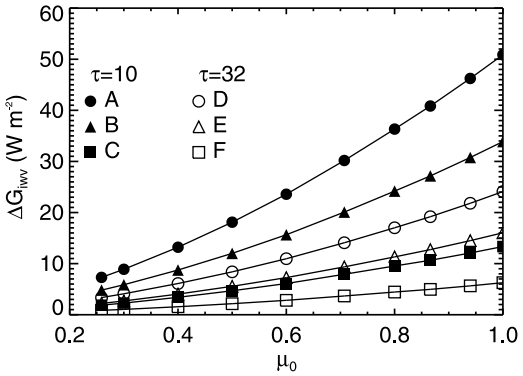

Figure 8. Sensitivity of the global irradiance to integrated water vapor column (IWV) as a function of μ_0. ΔG_{iwv} is the difference between the global irradiance calculated with IWV = 0.5 (circles labeled A and D), 1 (triangles labeled B and E), and 2 cm (squares labeled C and F) and the global irradiance calculated with IWV = 2.96 cm, for cloud optical thickness of 10 (symbols A-C) and 32 (symbols D-F). r_e = 8 μm.

polluted clouds is usually smaller than in clean clouds [*Miles et al.*, 2000]. *Peng et al.* [2002] showed that the effective radius measured from stratiform water clouds in the RACE and FIRE.ACE campaigns was 4.2 ± 1.4 μm for polluted cloud cases and was 9.0 ± 2.3 μm for clean cloud cases. For our cloud cases the smallest r_e is 6.5 μm, which suggests that the clouds are not very polluted.

[50] Figure 7 shows the differences between calculated global irradiances with aerosols and without aerosols, ΔG_{aer} (= $G_{aer} - G_{ref}$), for COT = 10 and 32, respectively, as a function of μ_0. The G_{aer} values are taken from the aerosol correction LUT with AOT of 0.1, 0.2 and 0.3. With aerosols the simulated global irradiances are smaller than without aerosols. As shown in Figure 7, at μ_0 = 0.5, the largest ΔG_{aer} is about −6 W/m^2. The absolute differences are larger at large μ_0 and low COT, because the irradiances are larger. The relative differences are larger at small μ_0 (not shown in Figure 7) and large COT because the light paths are longer at small μ_0 and large COT. The radiative effect of aerosols in cloudy skies occurs mainly due to the absorption by aerosols, which causes a lower total single scattering albedo of the cloud layer than that of clean clouds (without aerosols). Small absorptions are amplified because of long light paths due to the multiple scattering processes inside clouds. For the same μ_0, COT and r_e, the aerosol effect ΔG_{aer} is nearly a linear function of AOT (see Figure 7), and therefore we can easily correct for the aerosol effect if the AOT is known from measurements or a climatology.

[51] To further test the effect of aerosol absorption on the global irradiance of cloudy skies, we changed the aerosol profile and thereby the total SSA of the cloud layer. We thereto calculated the global irradiances, G_{aer_new}, with different aerosol settings, namely AOT = 0.2 at 500 nm, in the boundary layer RH = 70% and VIS = 23 km, and in the free troposphere RH = 70% and VIS = 23 km. For COT = 10 and r_e = 10 μm, these new aerosol settings led to a total cloud layer SSA of 0.99916 at 554.8 μm, while the total cloud layer SSA is of 0.99973 for the standard aerosol settings used for the LUT of G_{aer}. So there is more absorption in the cloud layer with the new aerosol settings than with the standard aerosol settings. For the same cloud (COT = 10 and r_e = 10 μm) at μ_0 = 0.5, ΔG_{aer_new} (= $G_{aer\_new} - G_{ref}$) is −6.7 W/m^2 while the corresponding ΔG_{aer} is −4.0 W/m^2. This confirms that the aerosol properties, such as AOT and SSA, are of importance if we aim for an accuracy of a few W/m^2 in the radiative closure of cloudy skies. The lack of simultaneous aerosol measurements is a shortcoming of this cloudy closure study.

4.3. Effect of Water Vapor

[52] The effect of water vapor on the global irradiance of cloudy skies is shown in Figure 8. There the differences between global irradiances (G_{iwv}) with IWV = 0.5, 1, 2 cm and global irradiances (G_{ref}) with IWV = 2.96 cm, denoted by $\Delta G_{iwv} = G_{iwv} - G_{ref}$, is plotted as a function of μ_0. For a cloudless atmosphere, the water vapor column has almost no effect on the diffuse irradiance [*Wang et al.*, 2009a]. The effect of water vapor on the global irradiance for cloudy atmospheres is due to the enhanced light path in the cloud and therefore enhanced absorption by water vapor. Because of the enhanced water vapor absorption, the global irradiance is always reduced. The largest ΔG_{iwv} occurs at large μ_0 and small COT because the global irradiances are largest there. Within the measured IWV and AOT ranges in Cabauw in this closure study, which are IWV of [0.7, 3.1] cm and AOT of [0.1, 0.3], ΔG_{iwv} is usually larger than ΔG_{aer} in absolute value.

4.4. Uncertainties due to Separated Aerosol and Water Vapor Corrections

[53] In principle, the global irradiance is a function of the variables μ_0, COT, r_e, IWV, and AOT. In the aerosol and water vapor correction LUTs we varied AOT and IWV separately and assumed a fixed value for IWV (2.96 cm) when calculating G_{aer} and a fixed value for AOT (0) when calculating G_{iwv}. The advantages of separated corrections are the reductions in calculation time and size of the LUTs. However, we have to demonstrate that the separation of aerosol and water vapor corrections does not introduce a

Table 4. Summary of the Experiments for the Uncertainty of Separated Aerosol and Water Vapor Corrections[a]

	Experiment											
	A: $\Delta G_{iwvaer} = G_{iwvaer}$(AOT = 0, IWV = x) − G_{iwvaer}(AOT = 0.2, IWV = x)						B: $\Delta G_{iwvaer} = G_{iwvaer}$(IWV = 1, AOT = y) − G_{iwvaer}(IWV = 4, AOT = y)					
	1	2	3	4	5	6	1	2	3	4	5	6
x (cm)	0.5	2	4	0.5	2	4	–	–	–	–	–	–
y	–	–	–	–	–	–	0	0.1	0.2	0	0.1	0.2
COT	10	10	10	32	32	32	10	10	10	32	32	32

[a]The effective radius is 8 μm for the experiments.

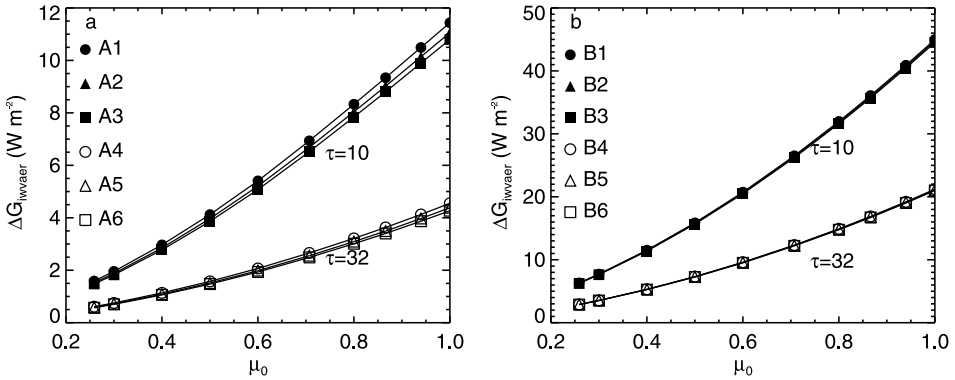

Figure 9. Sensitivity of the global irradiance to a simultaneous variation of IWV and AOT. (a) $\Delta G_{\mathrm{iwvaer}}$ is the difference in global irradiance between AOT = 0 and 0.2 for cases with IWV = 0.5 (circles labeled A1 and A4), 2 (triangles labeled A2 and A5), and 4 (squares labeled A3 and A6) cm. (b) $\Delta G_{\mathrm{iwvaer}}$ is the difference in global irradiance between IWV = 1 and 4 cm for cases with AOT = 0 (circles labeled B1 and B4), 0.1 (triangles labeled B2 and B5), and 0.2 (squares labeled B3 and B6). Cloud optical thickness is 10 and 32. r_e = 8 μm.

large error. Therefore, we calculated the global irradiances with all the possible aerosol, water vapor and cloud combinations, denoted by G_{iwvaer}, using AOT = 0.1, 0.2, 0.3, IWV = 0.5, 1, 2, 4 cm, COT = 10 and 32, and r_e = 8 μm. Two numerical experiments, A and B, were designed to test the effects of IWV on ΔG_{aer} and the effect of AOT on ΔG_{iwv}. The experiments are summarized in Table 4. For experiment A, G_{iwvaer} was calculated for COT = 10 (cases A1–A3) and 32 (cases A4–A6) with r_e = 8 μm to represent thin and thick clouds. For each COT, $\Delta G_{\mathrm{iwvaer}} = G_{\mathrm{iwvaer}}(\mathrm{AOT} = 0, \mathrm{IWV} = x) - G_{\mathrm{iwvaer}}(\mathrm{AOT} = 0.2, \mathrm{IWV} = x)$ was calculated using x = 0.5, 2, and 4 cm. Figure 9a shows the results for $\Delta G_{\mathrm{iwvaer}}$ as a function of μ_0. Indeed, for the cases with the same COT, $\Delta G_{\mathrm{iwvaer}}$ values calculated with different IWV are very similar for given μ_0. The effect of IWV on $\Delta G_{\mathrm{iwvaer}}$ decreases with the decrease of μ_0 and is smaller for thick clouds than for thin clouds. The uncertainty for aerosol correction with a fixed IWV = 2.96 cm is overall less than 1 W/m^2 and less than 0.5 W/m^2 for small μ_0.

[54] The same approach was used to test the impact of the AOT on the correction of IWV for G_{ref}. For experiment B, $\Delta G_{\mathrm{iwvaer}}$ was calculated for COT = 10 (cases B1–B3) and 32 (cases B4–B6), with r_e = 8 μm. For each COT, $\Delta G_{\mathrm{iwvaer}} = G_{\mathrm{iwvaer}}(\mathrm{IWV} = 1, \mathrm{AOT} = y) - G_{\mathrm{iwvaer}}(\mathrm{IWV} = 4, \mathrm{AOT} = y)$ was calculated using y = 0, 0.1, and 0.2. Figure 9b shows the results for $\Delta G_{\mathrm{iwvaer}}$ as a function of μ_0. For the experiments with the same COT, $\Delta G_{\mathrm{iwvaer}}$ values calculated with different AOT are very similar for a given μ_0. The effect of AOT on $\Delta G_{\mathrm{iwvaer}}$ is less than 0.5 W/m^2. The results show that the correction of G_{ref} for water vapor using a fixed AOT is accurate and that the uncertainty due to the chosen correction approach, with AOT = 0, is small. The numerical results in Figure 9 demonstrate that our approach of separated corrections of aerosols and water vapor for the reference global irradiances is appropriate. The uncertainty in the simulated global irradiances due to the separated correction approach is overall less than 1 W/m^2.

4.5. Effect of Surface Albedo

[55] In order to investigate the effect of the surface albedo on the global irradiance we simulated the global irradiances using surface albedo values from the three different grass spectra mentioned in section 2.2.4 (Grass-Fescue-Wheat YNP-FW-1, YNP-FW-2, YNP-FW-3). Here the grass spectra are noted as FW1, FW2, and FW3. The grass spectra FW1–FW3 and the grass spectrum used in the DAK LUT calculations (indicated as Org.) are shown in Figure 10a. For comparison, the climatological MERIS surface albedo spectra at Cabauw for January and July are also presented in Figure 10a. The original grass albedo spectrum used in DAK is comparable to the MERIS surface albedo spectra. The MERIS surface albedo spectrum is different in January and July and the seasonal variations of the MERIS surface albedo are also different at different wavelengths. For the wavelengths longer than 885 nm the original surface albedo values are lower than the values from the FW1–FW3 grass spectra. However, we do not have MERIS surface albedo values at these longer wavelengths.

[56] The differences between the global irradiances calculated using the grass reflectance spectra FW1–FW3 and the original grass spectrum, ΔG_{alb} (= $G_{\mathrm{alb}} - G_{\mathrm{ref}}$), are shown in Figure 10b for COT = 10 and 32, respectively, as a function of μ_0. The effective radius is 8 μm. In Figure 10b, cases A and D use grass spectrum FW1, cases B and E use grass spectrum FW2, and cases C and F use grass spectrum FW3. In general the absolute values of ΔG_{alb} are smaller at small μ_0 and become larger at large μ_0. The largest differences are [−9.7, 3.1] W/m^2 at μ_0 = 1, while at μ_0 = 0.5, the differences are [−3.3, 0.9] W/m^2. Using FW1 and FW2, ΔG_{alb} is similar for COT = 10 and 32. Using FW3, the absolute value of ΔG_{alb} is smaller for COT = 32 and larger for COT = 10. If the surface albedo is larger, the global irradiance is larger due to the enhanced multiple scattering and reflection between clouds and surface. ΔG_{alb} is negative for cases A, B, D, and E because the original surface albedo is brighter than the FW1 and FW2 spectra at the wavelengths shorter than 900 nm and the solar irradiance is larger in the UV and visible wavelengths than in the infrared. For cases C and F, the original surface albedo is lower than FW3 at wavelengths shorter than 700 nm and larger than FW3 at 700–900 nm; therefore ΔG_{alb} responds differently to thin and thick clouds. This sensitivity study suggests that the

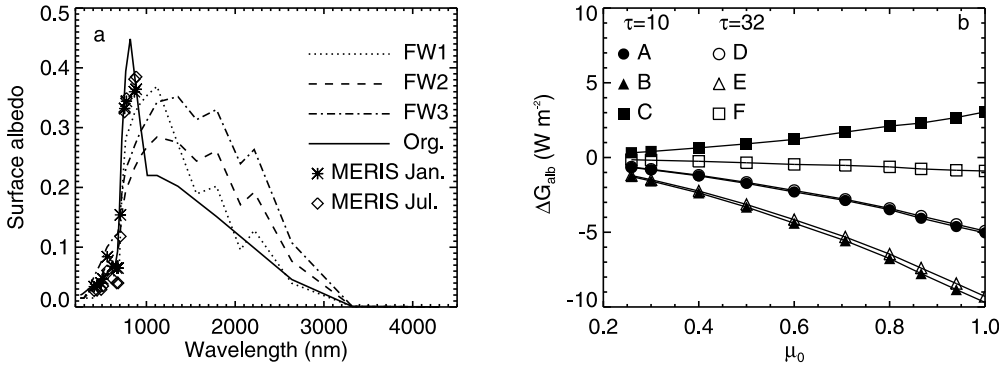

Figure 10. (a) The grass reflectance spectra FW1, FW2, and FW3; the surface albedo spectrum used to generate the LUTs ("Org."); and the MERIS surface albedo climatology for Cabauw in January and July. (b) Sensitivity of the global irradiance to surface albedo as a function of μ_0. ΔG_{alb} is the difference between the global irradiance calculated with grass reflectance spectrum FW1 (circles labeled A and D), FW2 (triangles labeled B and E), and FW3 (squares labeled C and F) and the global irradiance calculated from the reference LUT, for cloud optical thickness of 10 (symbols A-C) and 32 (symbols D-F). $r_e = 8$ μm.

surface albedo spectrum is important for an accurate simulation of the global irradiance for cloudy cases. This is even more relevant when realizing that the surface albedo has a seasonal dependence. A better solution for the surface albedo would be to use spectral albedo measurements at the same site. For example, a combined MERIS and MODIS surface albedo climatology covering the shortwave spectral range would be closer to the actual surface albedo than a surface albedo spectrum taken from a typical surface type. Because we do not have spectral surface albedo measurements of Cabauw for the full shortwave range, we could not correct the effect of the surface albedo on the global irradiances. For the cases on 30 January 2007 and 4 November 2008, μ_0 is relative small; therefore, we estimate that the effect of the surface albedo spectrum on the global irradiance is small.

4.6. Uncertainties in the Cloudy Sky Closure

[57] As we have discussed above, the largest errors in the cloudy sky irradiance calculations come from COT errors, so the errors of LWP and r_e are the main error sources in the closure study. The uncertainty in LWP and IWV from the MWR depends on the calibration of the channels used for the retrieval. The highest error occurs when both channels have an offset error of 1 K but with opposite sign, yielding a 31 g/m^2 (1 kg/m^2) error in the mean LWP (IWV) [*Crewell and Loehnert*, 2003]. Because calibration errors in the two channels are often positively correlated, it is favorable to have the same sign in both channels giving an overall error of 16 g/m^2 (0.4 kg/m^2) [*Crewell and Loehnert*, 2003]. The retrieval error in the MODIS r_e values can be 1–3 μm [*King et al.*, 1998]. The uncertainty of the AERONET AOT is about 0.01–0.02 [*Dubovik et al.*, 2000]. Here we use the standard deviation of the yearly mean AOT at Cabauw (0.1) as the uncertainty to account for the deviation of the yearly mean AOT from the actual AOT.

[58] Given the uncertainties and possible variations in LWP, r_e, IWV and AOT, we calculated global irradiances by varying these parameters separately, within their respective uncertainty limits, and compared the calculated irradiances with those of the reference case. The reference case has the mean parameters of all the selected cloud cases. The results of the sensitivity study are summarized in Table 5.

[59] Case 1 reflects the worst case uncertainty in the LWP, ±30 g/m^2; in our measurements the error is most probably not more than half of that uncertainty. Therefore case 2 shows the more reasonable uncertainty of LWP, ±16 g/m^2; the resulting changes in global irradiance are −10.2 and +11.8 W/m^2 at μ_0 = 0.42. Not only LWP, but also r_e influences COT. Therefore, in case 4 we estimate the change in global irradiance due to the influence of r_e on COT. By contrast, in case 3 r_e influences only the scattering matrix but not COT. For $r_e \pm 2$ μm, the changes in global irradiance are +2.2 and −3.7 W/m^2 in case 3 and +18.9 and −23.6 W/m^2 in case 4. Case 5 is similar to case 4 but with $r_e \pm 1$ μm, therefore the changes in global irradiance are

Table 5. Sensitivity of Global Irradiance (G) to Variations in LWP, r_e, COT, IWV, and AOT Within Their Uncertainty Limits[a]

Experiment	Parameter Variation	COT	$G - G_{ref}$ (W/m^2)		
			μ_0 = 0.259	μ_0 = 0.42	μ_0 = 0.866
1a	LWP + 30 g/m^2	25.9	−8.6	−17.5	−54.8
1b	LWP − 30 g/m^2	14.5	12.0	24.5	77.0
2a	LWP + 16 g/m^2	23.2	−5.0	−10.2	−32.0
2b	LWP − 16 g/m^2	17.1	5.8	11.8	37.0
3a	r_e + 2 μm	20.1	1.1	2.2	7.1
3b	r_e − 2 μm	20.1	−1.8	−3.7	−11.6
4a	r_e + 2 μm	16.1	9.2	18.9	59.6
4b	r_e − 2 μm	27.0	−11.5	−23.6	−74.0
5a	r_e + 1 μm	17.9	4.8	9.7	30.7
5b	r_e − 1 μm	23.1	−5.6	−11.4	−35.8
6a	COT + 0.1	20.2	−0.2	−0.4	−1.1
6b	COT − 0.1	20.0	0.2	0.4	1.1
7a	AOT + 0.1	20.1	−1.1	−2.2	−6.4
7b	AOT − 0.1	20.1	1.1	2.2	6.3
8a	IWV + 0.5 cm	20.1	−0.2	−0.3	−0.9
8b	IWV − 0.5 cm	20.1	0.2	0.3	0.9
Reference	–	20.1	64.44	129.95	399.10

[a]In the reference case LWP = 106.2 g/m^2, r_e = 7.9 μm, COT = 20.1, IWV = 1.9 cm, and AOT = 0.23. Global irradiance values for the reference case (G_{ref}) at μ_0 = 0.259, 0.42, 0.866 are 64.44, 129.95 and 399.10 W/m^2.

reduced to +9.7 and −11.4 W/m^2. In cases 6 and 7, the total optical thickness (COT + AOT) is varied by ±0.1, but case 6 involves a change of ±0.1 in COT, which causes mainly scattering, whereas case 7 involves a change of ±0.1 in AOT, which leads to more absorption. The global irradiance varies ±0.4 W/m^2 in case 6 and ±2.2 W/m^2 in case 7. These results clearly show that to simulate the global irradiance within a few W/m^2, not only the total optical thickness (AOT + COT) should be right, but also the aerosol absorption contribution should be correct. Finally, case 8 shows that the global irradiance error due to the uncertainty in IWV (±0.5 cm) is small (±0.3 W/m^2).

[60] Assuming the LWP error of ±16 g/m^2 (case 2), r_e error of ±1 μm (case 5), AOT error of ±0.1 (case 7), and IWV error of ±0.5 cm (case 8), we get a total calculated uncertainty of ±15 W/m^2 for the simulated global irradiance at $\mu_0 = 0.42$, which is very close to the uncertainty of the achieved closure ($\langle \Delta G \rangle$) of 14 W/m^2 (see section 3). Assuming larger errors in LWP and r_e, namely a LWP error of ±30 g/m^2 and a r_e error of ±2 μm, the total uncertainty of the simulated global irradiance becomes ±30 W/m^2 at $\mu_0 = 0.42$. So the uncertainty of the achieved closure is well within the measurement errors of the input parameters to the DAK model. Moreover, the mean difference between the simulated and measured global irradiances, being 6 W/m^2 (see section 3), is within the error of BSRN measurements (see section 2.4). Therefore, we can conclude that the closure is achieved and the DAK model is validated by the BSRN measurements for both clear-sky [*Wang et al.*, 2009a] and overcast, homogeneous, single-layer water cloud cases.

5. Conclusions

[61] A shortwave radiative closure analysis has been performed for overcast, single-layer, homogeneous water clouds over Cabauw, the Netherlands. The selection of cloudy sky cases, based on a large number of ground-based and satellite instruments, was a very important aspect of the cloudy radiative closure study. The selection of cloud cases was automatic and objective. The selected cases were overcast skies with nonprecipitating, single-layer water clouds. The homogeneity of the clouds was mainly checked from images; we did not have strict criteria for the homogeneity of clouds.

[62] In this closure study we used the Doubling-Adding KNMI (DAK) code for the simulation of global irradiances. Instead of simulating every case individually, we used a look-up table (LUT) approach. The reference irradiance LUT was generated with varied cloud properties and fixed integrated water vapor column and no aerosols. The deviations of actual water vapor and aerosols to the values used in the reference irradiance LUT were corrected using the water and aerosol correction LUTs. To reduce the size of the LUTs, we used the midlatitude summer atmospheric profile and scaled the water vapor profile to the actual integrated water vapor column. The cloud layer was fixed at 1–2 km. For the DAK simulations, the input data were taken from operational remote sensing products or climatological data: liquid water path and integrated water vapor column from microwave radiometers, effective radius from MODIS and aerosol information from the AERONET climatology. The LUT approach is suitable for the simulations of the global irradiances for these relatively simple cloud cases. The LUT approach is fast and can be applied to more cases and other sites.

[63] For 639 cloud cases on 9 days between May 2008 and May 2009 and on 30 January 2007, the mean difference between the simulated and measured global irradiances is 6 W/m^2 with a standard deviation of 14 W/m^2. The correlation coefficient is 0.949. For the best cases, such as on 4 November 2008, the mean difference between the simulated and measured global irradiances is 3 W/m^2 with a standard deviation of 8 W/m^2. Thus the global irradiances simulated by the DAK model have a very good agreement with the measured global irradiances and the closure is achieved. The good agreement between the simulated and measured global irradiances suggests that the uncertainty of the BSRN global irradiances could be better than ±9 W/m^2, especially for the mean of the global irradiances. Because the selected cloud cases span a large range of solar zenith angles (41–75°), cloud liquid water paths (30–400 g/m^2), and integrated water vapor columns (0.7–3.1 cm), the closure analysis covers the typical overcast homogeneous, single-layer, water cloud cases for Cabauw. The DAK radiative transfer model has been validated using BSRN measurements for both clear-sky and overcast homogeneous single-layer water cloud cases. This is only a first step for our model validation. We plan to perform more closure studies for other cloud types and at different BSRN sites. Then we can use DAK to validate the radiation calculations in climate models.

[64] We investigated the effects of cloud properties, aerosols, water vapor and surface albedo on the global irradiances and the radiative closure. The cloud optical thickness, derived from liquid water path and effective radius of cloud particles, is the most important piece of information for the closure study, because it largely determines the magnitude of the simulated global irradiances. In order to achieve a shortwave closure within a few W/m^2, high-quality water vapor and aerosol data are also needed. The impact of surface albedo on the cloudy closure could be of a similar magnitude as that of aerosols.

[65] In our closure study the main uncertainty is the effective radius, especially since we only have one or two measurements per day from MODIS. Even if the effective radius retrieval error can be neglected, the effective radius still has temporal and spatial variability. The achieved good closure is due to the relatively stable nature of stratiform clouds. The lack of aerosol and surface albedo measurements is another weakness of the closure study. The closure for the overcast cases could be improved in the following aspects: (1) use of retrieved effective radius information from suitable cloud radar measurements; (2) use of aerosol properties from in situ measurements on the ground; and (3) use of spectral surface albedo from combined MERIS and MODIS products, providing surface albedo values at more wavelengths in the shortwave. With these extra measurements the uncertainty of the closure could be further reduced.

[66] **Acknowledgments.** We are grateful to Marcel Brinkenberg, Cor van Oort, Jacques Warmer, and the measurement and infrastructure department of KNMI for operating and maintaining the BSRN site in Cabauw. We thank Mark Savenije (KNMI) for providing the cloud fraction data and the rain gauge precipitation flags. We thank Henk Klein Baltink

(KNMI) for providing the microwave radiometer data, Cloudnet data, and the helpful discussions about the data and the measurements. We thank Antonio Martelluci (ESA) for providing the microwave radiometer data. We acknowledge the Cloudnet project (European Union contract EVK2-2000-00611) for providing the Target Categorization product, which was produced by KNMI using measurements from the Cabauw Experimental Site for Atmospheric Research (CESAR). We thank Gerrit de Leeuw for his effort in establishing and maintaining the AERONET site in Cabauw. We also acknowledge the MODIS mission scientists and associated NASA personnel for the production of the data used in this research effort. This work was supported by the Dutch research program Climate Changes Spatial Planning (KvR) project CS02-P1. We thank the anonymous reviewers for the helpful comments and suggestions.

References

Ackerman, T. P., D. M. Flynn, and R. T. Marchand (2003), Quantifying the magnitude of anomalous solar absorption, *J. Geophys. Res.*, *108*(D9), 4273, doi:10.1029/2002JD002674.

Anderson, G. P., S. A. Clough, F. X. Kneizys, J. H. Chetwynd, and E. P. Shettle (1986), AFGL atmospheric constituent profiles, *Tech. Rep., AFGL-TR-86-0110*, Air Force Geophys. Lab., Hanscom AFB, Mass.

Boers, R., M. J. de Haij, W. M. F. Wauben, H. Klein Baltink, L. H. van Ulft, M. Savenije, and C. N. Long (2010), Optimized fractional cloudiness determination from five ground-based remote sensing techniques, *J. Geophys. Res.*, *115*, D24116, doi:10.1029/2010JD014661.

Bohren, G., J. R. Linskens, and M. E. Churma (1995), At what optical thickness does a cloud completely obscure the Sun?, *J. Atmos. Sci.*, *52*, 1257–1259, doi:10.1175/1520-0469(1995)052<1257:AWOTDA>2.0.CO;2.

Bowker, D. E., R. E. Davis, D. L. Myrick, K. Stacy, and W. T. Jones (1985), Spectral reflectances of natural targets for use in remote sensing studies, *NASA Ref. Rep.*, *1139*, 184 pp., Greenbelt, Md.

Brandau, C. L., H. W. J. Russchenberg, and W. H. Knap (2010), Evaluation of ground-based remotely sensed liquid water cloud properties using shortwave radiation measurements, *Atmos. Res.*, *96*, 366–377, doi:10.1016/j.atmosres.2010.01.009.

Chen, R., R. Wood, Z. Li, R. Ferraro, and F.-L. Chang (2008), Studying the vertical variation of cloud droplet effective radius using ship and space-borne remote sensing data, *J. Geophys. Res.*, *113*, D00A02, doi:10.1029/2007JD009596.

Clark, R. N., G. A. Swayze, R. Wise, E. Livo, T. Hoefen, R. Kokaly, and S. J. Sutley (2007), USGS digital spectral library splib06a, *Digital Data Ser.*, *231*, U.S. Geol. Surv., Denver, Colo. (Available at http://speclab.cr.usgs.gov/spectral.lib06.)

Crewell, S., and U. Loehnert (2003), Accuracy of cloud liquid water path from ground-based microwave radiometry: 2. Sensor accuracy and synergy, *Radio Sci.*, *38*(3), 8042, doi:10.1029/2002RS002634.

Crewell, S., K. Ebell, U. Löhnert, and D. D. Turner (2009), Can liquid water profiles be retrieved from passive microwave zenith observations?, *Geophys. Res. Lett.*, *36*, L06803, doi:10.1029/2008GL036934.

De Haan, J. F., P. B. Bosma, and J. W. Hovenier (1987), The adding method for multiple scattering computations of polarized light, *Astron. Astrophys.*, *183*, 371–391.

De Martino, G., B. van Ulft, H. ten Brink, M. Schaap, E. van Meijgaard, and R. Boers (2008), An aerosol-cloud module for inclusion in the KNMI regional climate model RACMO2, *KNMI-Publ., WR-2008-05*, R. Neth. Meteorol. Inst., De Bilt, Netherlands. (Available at http://www.knmi.nl/bibliotheek/knmipubWR/WR2008-05.pdf)

De Rooij, W. A., and C. C. A. H. van der Stap (1984), Expansion of Mie scattering matrices in generalized spherical functions, *Astron. Astrophys.*, *131*, 237–248.

Diem, M. (1948), Messungen der Grosse von Wolkenelementen II, *Meteorol. Rundsch.*, *1*, 261–273.

Dubovik, O., A. Smirnov, B. N. Holben, M. D. King, Y. J. Kaufman, T. F. Eck, and I. Slutsker (2000), Accuracy assessments of aerosol optical properties retrieved from Aerosol Robotic Network (AERONET) Sun and sky radiance measurements, *J. Geophys. Res.*, *105*, 9791–9806, doi:10.1029/2000JD900040.

Hansen, J. E. (1971), Multiple scattering of polarized light in planetary atmospheres. Part II. Sunlight reflected by terrestrial water clouds, *J. Atmos. Sci.*, *28*, 1400–1426, doi:10.1175/1520-0469(1971)028<1400:MSOPLI>2.0.CO;2.

Illingworth, A. J., et al. (2007), Cloudnet: Continuous evaluation of cloud profiles in seven operational models using ground-based observations, *Bull. Am. Meteorol. Soc.*, *88*, 883–898, doi:10.1175/BAMS-88-6-883.

Kato, S., T. P. Ackerman, J. H. Mather, and E. E. Clothiaux (1999), The k-distribution method and correlated-k approximation for a shortwave radiative transfer model, *J. Quant. Spectrosc. Radiat. Transfer*, *62*, 109–121, doi:10.1016/S0022-4073(98)00075-2.

King, M. D., S.-C. Tsay, S. E. Platnick, M. Wang, and K.-N. Liou (1998), Cloud retrieval algorithms for MODIS: Optical thickness, effective particle radius, and thermodynamic phase. Products: MOD06, MOD08, *ATBD Ref. ATBD-MOD-05*, NASA Goddard Space Flight Cent., Greenbelt, Md.

Knap, W. H. (2008), Basic measurements of radiation at station Cabauw (2008–05), report, doi:10.1594/PANGAEA.703322, K. Ned. Meteorol. Inst., De Bilt, Netherlands.

Kneizys, F. X., E. P. Shettle, L. W. Abreu, J. J. Chetwynd, G. P. Anderson, W. O. Gallery, J. E. A. Selby, and S. A. Clough (1988), Users guide to LOWTRAN 7, *Tech. Rep., AFGL-TR-88-0177*, Air Force Geophys. Lab., Bedford, Mass.

Kuipers Munneke, P., C. H. Reijmer, M. R. van den Broeke, G. König-Langlo, P. Stammes, and W. H. Knap (2008), Analysis of clear-sky Antarctic snow albedo using observations and radiative transfer modeling, *J. Geophys. Res.*, *113*, D17118, doi:10.1029/2007JD009653.

Loehnert, U., and S. Crewell (2003), Accuracy of cloud liquid water path from ground-based microwave radiometry: Part I. Dependency on cloud model statistics and precipitation, *Radio Sci.*, *38*(3), 8041, doi:10.1029/2002RS002654.

Mace, G. G., et al. (2006), Cloud radiative forcing at the Atmospheric Radiation Measurement Program Climate Research Facility: 1. Technique, validation, and comparison to satellite-derived diagnostic quantities, *J. Geophys. Res.*, *111*, D11S90, doi:10.1029/2005JD005921.

McArthur, L. J. B. (2004), Baseline Surface Radiation Network (BSRN) operations manual—Version 2.1, *WMO/TD Rep. 879*, World Clim. Res. Programme, World Meteorol. Organ., Geneva, Switzerland.

McFarlane, S. A., and K. F. Evans (2004), Clouds and shortwave fluxes at Nauru. Part II: Shortwave flux closure, *J. Atmos. Sci.*, *61*, 2602–2615, doi:10.1175/JAS3299.1.

Michalsky, J. J., G. P. Anderson, J. Barnard, J. Delamere, C. Gueymard, S. Kato, P. Kiedron, A. McComiskey, and P. Ricchiazzi (2006), Shortwave radiative closure studies for clear skies during the Atmospheric Radiation Measurement 2003 Aerosol Intensive Observation Period, *J. Geophys. Res.*, *111*, D14S90, doi:10.1029/2005JD006341.

Miles, N. L., J. Verlinde, and E. E. Clothiaux (2000), Cloud droplet size distributions in low-level stratiform clouds, *J. Atmos. Sci.*, *57*, 295–311, doi:10.1175/1520-0469(2000)057<0295:CDSDIL>2.0.CO;2.

Nowak, D., L. Vuilleumier, and A. Ohmura (2008), Radiation transfer in stratus clouds at the BSRN Payerne site, *Atmos. Chem. Phys. Discuss.*, *8*, 11,453–11,485, doi:10.5194/acpd-8-11453-2008.

Ohmura, A., et al. (1998), Baseline Surface Radiation Network (BSRN/WCRP): New precision radiometry for climate research, *Bull. Am. Meteorol. Soc.*, *79*(10), 2115–2136, doi:10.1175/1520-0477(1998)079<2115:BSRNBW>2.0.CO;2.

Oreopoulos, L., and E. Mlawer (2010), The continual intercomparison of radiation codes (CIRC): Assessing anew the quality of GCM radiation algorithms, *Bull. Am. Meteorol. Soc.*, *91*, 305–310, doi:10.1175/2009BAMS2732.1.

Peng, Y., U. Lohmann, R. Leaitch, C. Banic, and M. Couture (2002), The cloud albedo-cloud droplet effective radius relationship for clean and polluted clouds from RACE and FIRE.ACE, *J. Geophys. Res.*, *107*(D11), 4106, doi:10.1029/2000JD000281.

Platnick, S. (2000), Vertical photon transport in cloud remote sensing problems, *J. Geophys. Res.*, *105*, 22,919–22,935, doi:10.1029/2000JD900333.

Popp, C., P. Wang, D. Brunner, P. Stammes, Y. Zhou, and M. Grzegorski (2011), MERIS albedo climatology for FRESCO+ O_2 A-band cloud retrieval, *Atmos. Meas. Tech.*, *4*, 463–483, doi:10.5194/amt-4-463-2011.

Rose, T., S. Crewell, U. Loehnert, and C. Simmer (2005), A network suitable microwave radiometer for operational monitoring of the cloudy atmosphere, *Atmos. Res.*, *75*, 183–200, doi:10.1016/j.atmosres.2004.12.005.

Schmetz, J. (1993), Relationship between solar net radiative flux at the top of the atmosphere and at the surface, *J. Atmos. Sci.*, *50*, 1122–1132, doi:10.1175/1520-0469(1993)050<1122:RBSNRF>2.0.CO;2.

Segelstein, D. (1981), The complex refractive index of water, M.S. thesis, Univ. of Mo., Kansas City.

Sengupta, M., E. E. Clothiaux, T. P. Ackerman, S. Kato, and Q.-L. Min (2003), Importance of accurate liquid water path for estimation of solar radiation in warm boundary layer clouds: An observational study, *J. Clim.*, *16*, 2997–3009, doi:10.1175/1520-0442(2003)016<2997:IOALWP>2.0.CO;2.

Shettle, E., and R. Fenn (1979), Models for the aerosols of the lower atmosphere and the effects of humidity variations on their optical properties, *Environ. Res. Pap.*, *676*, Air Force Geophys. Lab., Hanscom AFB, Mass.

Shi, Y., and C. N. Long (2002), Techniques and methods used to determine the best estimate of radiation fluxes at SGP central facility, paper presented at the Twelfth ARM Science Team Meeting, U.S. Dep. of Energy, Richland, Wash.

Stammes, P. (2001), Spectral radiance modelling in the UV-visible range, in *IRS 2000: Current Problems in Atmospheric Radiation*, edited by W. L. Smith and Y. M. Timofeyev, pp. 385–388, A. Deepak, Hampton, Va.

Stephens, G. L. (1978), Radiation profiles in extended water clouds, II: Parameterization scheme, *J. Atmos. Sci.*, *35*, 2123–2132, doi:10.1175/1520-0469(1978)035<2123:RPIEWC>2.0.CO;2.

Stephens, G. L. (2005), Cloud feedbacks in the climate system: A critical review, *J. Clim.*, *18*, 237–273, doi:10.1175/JCLI-3243.1.

Stephens, G. L., and S. C. Tsay (1990), On the cloud absorption anomaly, *Q. J. R. Meteorol. Soc.*, *116*, 671–704, doi:10.1002/qj.49711649308.

Wang, P., W. H. Knap, P. Kuipers Munneke, and P. Stammes (2009a), Clear-sky shortwave radiative closure for the Cabauw Baseline Surface Radiation Network site, the Netherlands, *J. Geophys. Res.*, *114*, D14206, doi:10.1029/2009JD011978.

Wang, P., W. H. Knap, P. Kuipers Munneke, and P. Stammes (2009b), Clear-sky atmospheric radiative transfer: A model intercomparison for shortwave irradiances, in *Current Problems in Atmospheric Radiation (IRS 2008), Proceedings of the International Radiation Symposium (IRC/IAMAS)*, edited by T. Nakajima and M. A. Yamasoe, pp. 125–128, Springer, New York.

Wauben, W. (2006), Evaluation of the Nubiscope, *KNMI Tech. Rep., TR-291*, R. Neth. Meteorol. Inst., De Bilt, Netherlands. (Available at http://www.knmi.nl/bibliotheek/knmipubTR/TR291.pdf.)

W. H. Knap, P. Stammes, and P. Wang, Royal Netherlands Meteorological Institute, Wilhelminalaan 10, NL-3732 GK, De Bilt, Netherlands. (wangp@knmi.nl)